NANO LETTERS

pubs.acs.org/NanoLett Letter

Interplay of Electrostatic Dipoles and Monopoles with Elastic Interactions in Nematic Liquid Crystal Nanocolloids

Blaise Fleury, Bohdan Senyuk, Mykola Tasinkevych, and Ivan I. Smalyukh*

Cite This: https://dx.doi.org/10.1021/acs.nanolett.0c02087 Read Online

ACCESS | Metrics & More | Article Recommendations | Supporting Information

ABSTRACT: Doping of nematic liquid crystals with colloidal nanoparticles presents a rich soft matter platform for controlling material properties and discovering diverse condensed matter phases. We describe nematic nanocolloids that simultaneously exhibit strong electrostatic monopole and dipole moments and yield competing long-range anisotropic interactions. Combined with interactions due to orientational elasticity and order parameter gradients of the nematic host medium, they lead to diverse forms of self-assembly both in the bulk of an aligned liquid crystal and when one-dimensionally confined by singular topological defect lines. Such nanocolloids exhibit facile responses to electric fields. We demonstrate electric reconfigurations of nanocolloidal pair-interactions and discuss how our findings may lead to realizing ferroelectric and dielectric molecular-colloidal fluids with different point group symmetries.

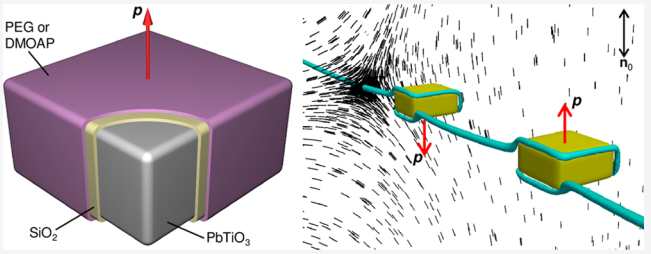

KEYWORDS: *Nanoparticle, interaction, liquid crystal, defect line, nematic colloid, ferroelectric, lead titanate*

Electrostatic interactions are ubiquitous in biological and soft matter systems, ranging from polyelectrolytes like proteins, DNA, and filamentous actin to inorganic colloidal nanoparticles with various forms of protonation or functionalization of surfaces.[1−5] These interactions are typically strongly screened by counterions present in respective fluid host media.[2] Charging of colloids and polyelectrolytes is often spatially inhomogeneous, like in the case of proteins and colloidal particles with specially designed patchy surfaces, so that the screened electrostatic interactions have not just Coulomb-like but also dipolar and higher-order multipole contributions.[1−5] In nematic liquid crystal (LC) colloids,[6,7] different types of elastic monopoles and multipoles have been identified too,[8−10] where the distortions of molecular alignment around colloidal inclusions, described by a nonpolar director field $\mathbf{n}(\mathbf{r}) \equiv -\mathbf{n}(\mathbf{r})$, are also represented in terms of multipole expansions.[11] Magnetically monodomain colloidal particles can both enable facile magnetic switching and lead to polar ferromagnetic LC fluids,[12,13] as envisaged in pioneering works of de Gennes and Brochard.[14] Moreover, electrostatic monopole-like interactions were shown as being capable of stabilizing various nematic colloidal low-symmetry crystalline and LC systems.[15,16] Separately, ferroelectric nanoparticles dispersed in LCs were shown enhancing dielectric responses and altering order−disorder transitions.[17,18] However, the rich behavior of such soft matter systems has not been studied at the level of individual particles and remains poorly understood, the simultaneous presence and interplay of electrostatic monopoles and dipoles has not been reported, and no ferroelectric analogs of ferromagnetic LCs[12,13] have been found so far.

Here, we describe the physical behavior of nematic colloids formed by rectangular-prism-shaped nanoparticles with strong electrostatic monopole and dipole moments. In the nonpolar LC medium, these particles exhibit long-range competing electrostatic interactions that are further enriched by shorter-range medium-mediated interactions due to the LC's orientational elasticity.[6,7,19] Weak electric fields, well below the nematic realignment threshold, reconfigure these interactions by changing relative orientations of electrostatic dipoles. Confinement of nanoparticles within singular defect lines allows us to unambiguously demonstrate that both electrostatic monopole and dipole moments play roles in defining long-range interactions and self-assembly. While proteins and patchy particles can also exhibit combinations of Coulomb and dipolar electrostatic interactions,[3−5] these interactions in LCs are long-ranging and reconfigurable by external fields. Our findings open a broad spectrum of possibilities for designing and realizing soft materials and condensed matter phases with facile electric responses to fields.

Received: May 19, 2020
Revised: September 30, 2020

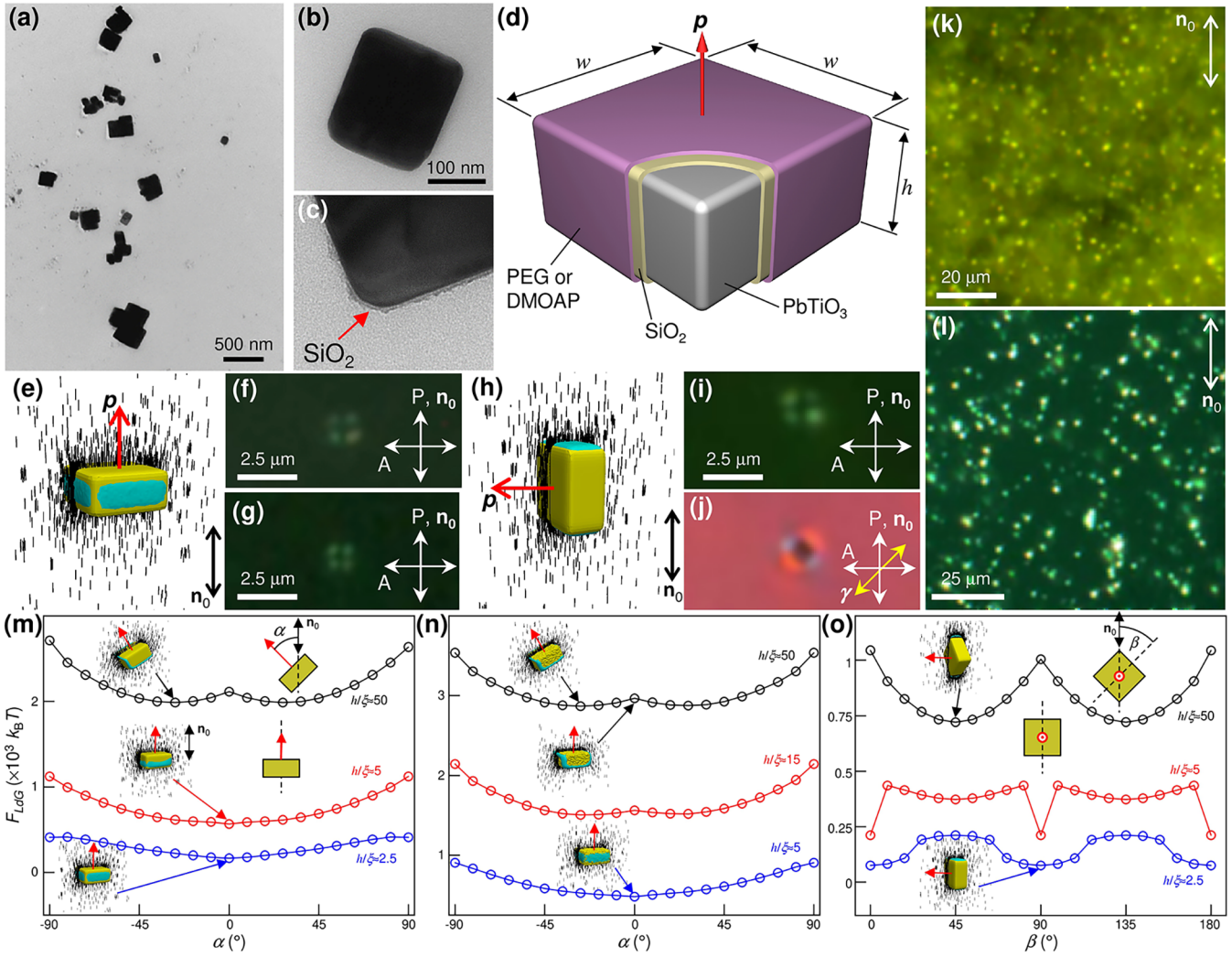

Figure 1. Ferroelectric nanoparticles in LCs. (a–c) TEM images of nanoparticles, with a thin silica coating indicated in (c). (d) Structure and geometry of a nanoparticle. (e,h) Computer-simulated director field $\mathbf{n}(\mathbf{r})$ (shown by black rods) around nanoparticles with (e) homeotropic and (h) tangential boundary conditions. Cyan isosurfaces depict regions of a reduced scalar-order parameter relative to its bulk value by 33%. (f,g,i,j) Polarizing micrographs of a bare nanoparticle (g) and nanoparticles with homeotropic (f) and tangential (i,j) boundary conditions in a planar cell without (f,g,i) and with (j) a retardation plate with a slow axis marked by "γ". (k,l) Dark field micrographs of nanoparticles with tangential boundary conditions dispersed in LC at different magnifications, with the zooming-in (l) showing polydispersity of distance r within colloidal assembles. (m–o) Computer-simulated elastic free energy of ferroelectric nanocolloids with homeotropic (m,n) and tangential (o) boundary conditions and different anchoring strengths versus their orientations relative to the far-field director $\mathbf{n}_0$; nanoparticles with smooth and nanoscale-rough surfaces are shown in (m,o) and (n), respectively. The angles describing nanoparticle orientations are defined in the insets. Insets also show representative orientations of the nanocolloids and corresponding $\mathbf{n}(\mathbf{r})$-configurations obtained by means of the numerical modeling.

We obtained $PbTiO_3$ platelets using a hydrothermal synthesis modified from ref 20. Lead nitrate $Pb(NO_3)_2$ and TiO_2 were mixed to a Pb:Ti molar ratio of 1.25:1 in a 7 M KOH aqueous solution in a 30 mL autoclave Teflon liner ([Pb] = 0.2 M). After sealing the autoclave, the sample was heated to 200 °C for 12 h, then cooled down and washed with 1% nitric acid in water, then with water, and finally with ethanol. An electric dipole moment $p = (0.5–2) \times 10^{-22}$ Cm was directed normal to the nanoparticle's base.[21] Synthesized polydisperse $PbTiO_3$ nanoparticles were size-selected through centrifugations (Figures 1a–d, and S1 and S2). Size-selected nanoparticles had a square $w \times w$ base and a height h, where $w = 2h \approx 100–120$ nm (Figures 1d and S1 and S2). To set boundary conditions on surfaces of $+(100–300)e$-charged particles, they were functionalized with [3-(trimethoxysilyl) propyl]octadecyl-dimethylammonium chloride (DMOAP) for homeotropic and poly(ethylene glycol) (PEG) for planar anchoring.[13] Briefly, 250 μL of 3 wt % $PbTiO_3$ nanoparticle dispersion was added to 250 mg of aqueous polyvinylpyrrolidone (40 kDa). After 24 h under stirring, the sample was washed by centrifugation and redispersed in 10 mL of ethanol. To grow a 3–4 nm layer of silica over nanoparticles, we added 350 μL of 28% NH_4OH, swiftly followed by the addition of 12.2 μL of tetraethoxysilane (TEOS). The solution was left to stir for 12 h, then purified by centrifugation and redispersed in ethanol. We grafted either Methoxy PEG Silane (JemKem) or DMOAP (Sigma-Aldrich) ligand on the silica shell. For the latter, a few drops of DMOAP were added to a water/methanol dispersion of silica-coated nanoparticles. After 15 min of shaking, the solution was washed by centrifugation and redispersed in ethanol. For the PEG grafting, the pH of silica coated nanoparticle dispersion was adjusted to pH = 12 by

https://dx.doi.org/10.1021/acs.nanolett.0c02087
Nano Lett. XXXX, XXX, XXX–XXX

adding 28% NH_4OH (~1.5 mL in 6 mL of a sample). Then, 4 mL of this dispersion was added to a 1 mL PEG solution (25 mg of 5000 Methoxy PEG Silane dissolved in 1 mL of ethanol) and stirred at 35 °C overnight. The ensuing ferroelectric nanoparticles were washed twice in methanol, then redispersed in ethanol and mixed with a nematic 4-cyano-4′-pentylbiphenyl (5CB, from Frinton Laboratories, Inc.) (Figure 1e-l). The Debye screening length κ^{-1} = 300−1000 nm was estimated using impedance spectroscopy.[16]

Glass substrates were dip-coated in an aqueous (1 wt %) solution of DMOAP to induce homeotropic far-field director $\mathbf{n}_0$. Planar $\mathbf{n}_0$ was achieved by using unidirectionally rubbed thin films of spin-coated and baked polyimide PI2555 (HD MicroSystem). The gap between substrates was set by glass microfibers or capillaries of desired diameter. The LC-nanoparticle dispersions (Figure 1k,l) were filled into cells by capillary action in the LC phase and sealed with epoxy glue. Polarizing and dark-field microscopy was performed with an inverted microscope IX81, 100× oil objective with variable numerical aperture NA = 0.6−1.3, and a dark-field condenser U-DCW (NA = 1.2−1.4) (all from Olympus). Room-temperature Brownian motion was probed with a CCD camera (Flea, PointGrey) at a rate of 15 fps; positions of nanoparticles versus time were determined using tracking plugins of ImageJ (freeware from the National Institute of Health). TEM images were obtained with a FEI Tecnai T12 under 120 kV.

Nanoparticles with homeotropic or tangential boundary conditions form elastic quadrupoles with surface defects on side faces (Figure 1e,h) as observed with polarizing optical microscopy (Figure 1f,i,j). The presence of four bright lobes in the textures of $\mathbf{n}(\mathbf{r})$ around nanoparticles (Figure 1f,i,j) is consistent with numerically calculated configurations of $\mathbf{n}(\mathbf{r})$ (Figures 1e,h,m−o and S3). Polarizing optical images of bare nanoparticles (Figure 1g) and nanoparticles with tangential or homeotropic boundary conditions show similar features in micrographs due to nanoscale colloidal dimensions and producing quadrupolar-type distortions in all these cases (Figures 1e,h,m−o, 2, and S3), which are responsible for elasticity-mediated interactions arising from minimization of the energetic costs due to these distortions.

Ferroelectric nanocolloids were stabilized against aggregation (Figure 1k,l) by the effective surface charge of Ze = (100−300)e per particle estimated using electrophoresis (Figure 3a−d) when applying electric field $\mathbf{E}\|\mathbf{n}_0$, where $e = 1.6 \times 10^{-19}$ C is an elementary charge. The surface charge was estimated after capping nanoparticles with alignment agents. The effective surface charge of individual nanoparticles was estimated from the velocity of the nanoparticle's electrophoretic motion in the nematic LC when samples were subjected to an external DC electric field $\mathbf{E}$ (Figure 3c). We used planar nematic cells with in-plane electrodes ~1 mm apart. Thin aluminum foil stripes (~30 μm in thickness) were used as electrodes, serving also as spacers separating glass substrates and defining the cell gap. A very dilute dispersion of nanoprisms in the nematic LC was infiltrated into the cell. When a DC voltage U = 1−10 V_{DC} was applied between the in-plane electrodes, nanoparticles moved toward a negative electrode, consistent with the fact that they are positively charged. The motion of nanoparticles was videorecorded and spatial displacements l versus time (Figure 3d) were extracted from videos using ImageJ, allowing us to calculate corresponding velocities of nanoparticles. The effective surface charge of the nanoparticle moving under the influence of an external electric field $E = U/d$ (note that the system is characterized by low Reynolds numbers) with a speed v was estimated from the balance of a viscous drag force $F_S = c_f v$ and an electrostatic force $F_{el} = (Ze)E$ acting on nanoparticles, which yields $Ze = c_f v d/U$, where d is the distance between electrodes.[15] The friction coefficient c_f was calculated from a diffusion constant D_f using the Einstein relation $c_f = k_B T/D_f$. In order to estimate D_f, we have probed the Brownian motion of a single nanoparticle in the LC host (Figure 3a,b) using videomicroscopy and image analysis, as described in detail elsewhere.[15,22]

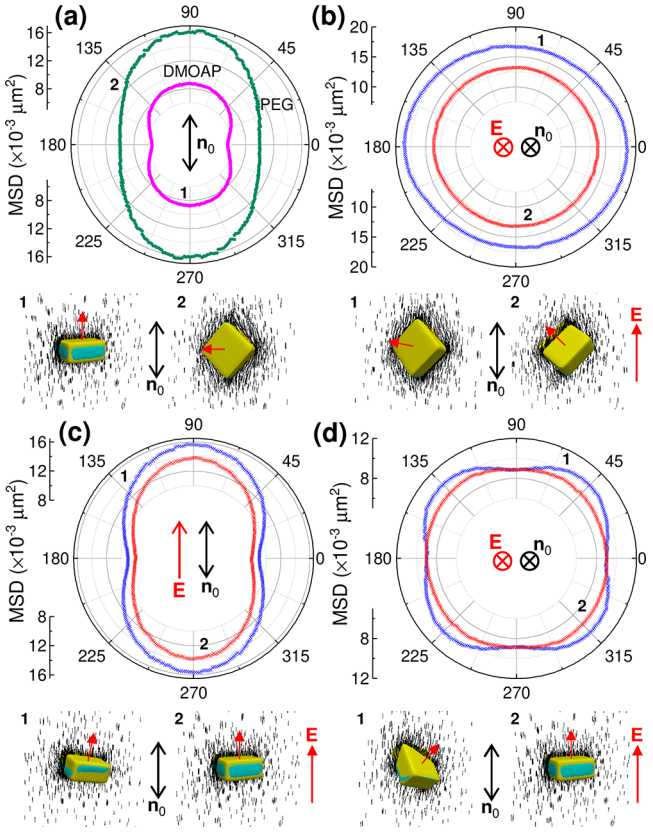

Figure 2. Diffusion of ferroelectric nanoparticles in LCs. (a) Orientational dependence of MSD of nanoparticles with homeotropic (1) and tangential (2) boundary conditions in a planar cell without an electric field. (b) Orientational dependence of MSD of a nanoparticle with tangential boundary conditions in a homeotropic cell without (blue) and with (red) E = 50 mV/μm. (c,d) MSD of bare nanoparticles in a planar (c) and homeotropic (d) cell without (blue) and with (red) applied field of E = 50 mV/μm. Insets 1 and 2 show corresponding numerically simulated visualizations of ferroelectric nanocolloids and their orientations with respect to $\mathbf{n}_0$ arising from the competition of elastic and electrostatic effects. The lag time used in videomicroscopy characterization was t = 67 ms in all plots.

The topography of silica-coated nanoparticles provides the opportunity for assessing effects of silica shell nanoscale roughness (Figures 1c,n and S3c,d) on the surface alignment and $\mathbf{n}(\mathbf{r})$-distortions when roughness length scales are much smaller than the surface extrapolation length $\xi = K/W_p \approx 0.1$ μm and even the nematic coherence length (~10 nm), where experimental parameters defining ξ as describing the competition of bulk elastic and surface anchoring effects are K ~10 pN, an average Frank elastic constant, and W_p ~10^{-4} J m^{-2}, a polar surface anchoring strength coefficient. Numerical modeling reveals only very minimal effects of the nanorough-

https://dx.doi.org/10.1021/acs.nanolett.0c02087
Nano Lett. XXXX, XXX, XXX−XXX

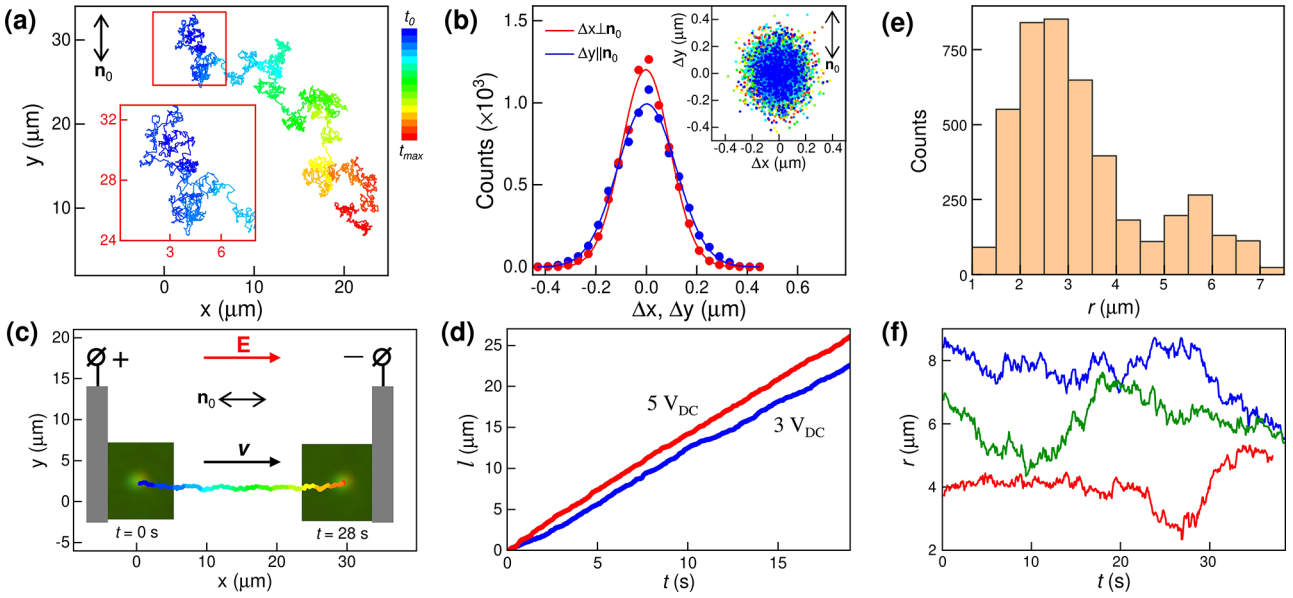

Figure 3. Characterization of ferroelectric nanoparticles with tangential boundary conditions in a planar LC cell. (a) Diffusion trajectory of a nanoparticle probed within ∼8 min at frame rate of 15 fps. Inset shows a zoomed-in view. Color shows the elapsed time from t_0 to t_{max} according to the color scale (right-side inset). (b) Histograms of displacements acquired with a lag time of t = 67 ms and showing anisotropy of diffusion. Inset depicts the in-plane displacements, with color-coded time according to the color scale shown in the inset of (a). (c,d) Electrophoresis of charged nanoparticles along **E** (c) probed at different DC voltages (d), which were used to determine surface charges of nanoparticles. (e) Histogram of separations between nanoparticles within dimer "assemblies at distance" and (f) separation between three pairs of nearest nanoparticles versus time (revealing that nanocolloidal interactions are comparable in strength to thermal fluctuations) in a concentrated colloidal dispersion shown in Figure 1k,l.

ness on the nanoparticle-induced $\mathbf{n}(\mathbf{r})$-structures and spatial regions of a reduced scalar order parameter (Figures 1m,n and S3a−d), which are only weakly sensitive to the presence of ∼1 nm topography as compared to the cases of atomically smooth surfaces of nanocolloids. Furthermore, edges and vertices of our nanoparticles do not tend to pin singular surface defect lines, which is different from what was previously observed for micrometer-sized nematic colloids with faceted surfaces.[23−25] This can be explained by the fact that our nanocolloids have a characteristic dimension h of 100 nm comparable to ξ, so that the competition of surface anchoring and bulk elastic effects corresponds to the regime of weak surface boundary conditions, when they can be violated (Figure 1m−o). This is different from previously studied faceted microparticles with dimensions orders of magnitude larger than ξ.[24,25] Numerical modeling (Figures 1m−o and S3) shows a crossover from a microcolloid (Figure S4) regime of faceted particles with defect lines localized near edges (found when $h/\xi \gg 1$) to a nanocolloid regime studied in this work ($h/\xi \approx 1$), when boundary conditions tend to be violated and regions of reduced scalar order parameter appear near locations of nanoparticles that have local easy axis direction not matching with $\mathbf{n}_0$. We shall see below, however, that edges of nanoparticles can affect the structure of accompanying defect lines when they are entrapped by such defects. The observed colloidal assemblies display polydispersity of interparticle center-to-center distances r because colloidal interactions between electrostatic dipoles depend on their relative orientations and strength as compared to elastic and monopole-type electrostatic interactions (Figures 1k,l and 3e,f). To unravel physical underpinnings of this behavior, we shall study their pair-interactions, including under one-dimensional confinement within defects.

While diffusion anisotropy in nematic colloids is observed even for spherical particles,[22] which is due to both the anisotropy of viscous properties of LCs and the structure of defects and $\mathbf{n}(\mathbf{r})$-distortions that accompany the particle (effectively making it shape-anisotropic),[22] our study reveals how this behavior can be both enriched and controlled through rotating the shape-anisotropic nanoparticles relative to $\mathbf{n}_0$ and through reconfiguring the corona of $\mathbf{n}(\mathbf{r})$-distortions and defects that nanoparticles induce within the LC host medium (Figures 2 and 3a,b). Ferroelectric nanoparticles with tangential or perpendicular boundary conditions (Figure 1e,h) undergo Brownian motion (Figure 3a) with a characteristic diffusion constant ratio $D_{\parallel}/D_{\perp} \approx 1.7$, where $D_{\parallel}$ and $D_{\perp}$ are diffusion coefficients measured parallel and perpendicular to $\mathbf{n}_0$, respectively (Figure 3b).[22] Diffusion of nanoparticles with perpendicular boundary conditions (DMOAP-treated) is weaker as compared to nanoparticles with tangential boundary conditions (PEG-treated) (Figure 2a and its insets), consistent with their orientation relative to the observation plane and $\mathbf{n}_0$, as well as the structure of perturbed nematic order and defects around them. The realignment of electrostatic colloidal dipoles (in cases when such dipoles are at initial orientations not parallel to the applied field) alters diffusion of nanoparticles (Figure 2b−d), even when applying a weak DC field E = 50−100 mV/μm along $\mathbf{n}_0$ that does not change $\mathbf{n}(\mathbf{r})$-orientation directly through its coupling with **E**. Polar plots (Figure 2b−d) of the nanoparticle's mean-square displacements (MSD) indicate significant changes of the diffusion coefficient with applying **E**, consistent with the rotation of a nanoparticle and the ensuing reconfiguration of the surrounding $\mathbf{n}(\mathbf{r})$-distortions due to the rotation of the nanoparticle's dipole moment **p** by **E**. The comparison of behavior of bare nanoparticles (Figure 2c,d) and the ones with surface treatment for tangential or perpendicular boundary conditions shows the importance of

https://dx.doi.org/10.1021/acs.nanolett.0c02087
Nano Lett. XXXX, XXX, XXX−XXX

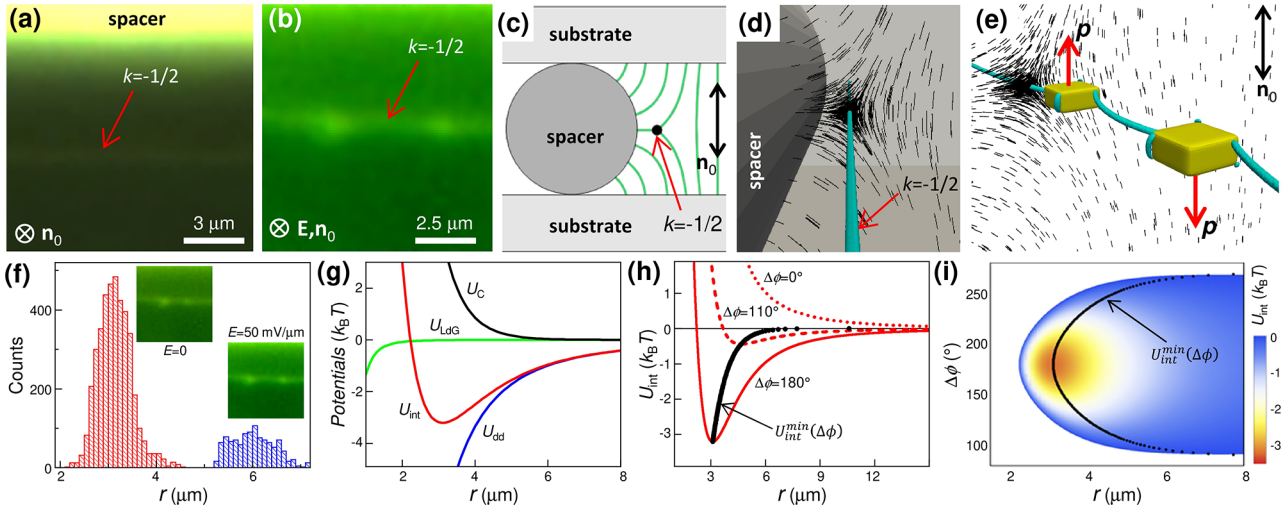

Figure 4. Electric control of interactions between ferroelectric nanoparticles with tangential boundary conditions entrapped by a defect line. (a,b) Dark-field micrographs of a half-integer disclination of winding number $k = -1/2$ in the vicinity of a round spacer (a), with two entrapped nanoparticles (b); this defect line is a topologically stable line defect labeled as $\pi_1(S^2/Z_2) = Z_2$, with the winding number k locally characterizing how many times the director rotates around a defect core when one circumnavigates it once. (c,d) Schematic diagram (c) and numerical simulation (d) of disclination's $\mathbf{n}(\mathbf{r})$. (e) Computer-simulated $\mathbf{n}(\mathbf{r})$ and defect line trapping two nanoparticles with tangential boundary conditions with antiparallel dipoles at the shortest r. (f) Histogram of separation between two nanoparticles with and without applied $\mathbf{E}$. (g) Pair-interaction potentials calculated based on experimental histograms (f) for nanoparticles with antiparallel alignment and computer-simulated U_{LdG}. (h) Total pair-interaction potentials for nanoparticles with antiparallel (red solid line for antiparallel dipoles with $\mathbf{p}$-orientations at $\Delta\phi = 180°$), misaligned (red dashed line at $\Delta\phi = 110°$), and parallel (red dotted line at $\Delta\phi = 0°$) electrostatic dipoles $\mathbf{p}$. Black symbols show the shifting minimum of U_{int} versus $\Delta\phi$ changing within 90−180°. (i) Energy-minimizing U_{int} versus $\Delta\phi$ and separation between nanoparticles.

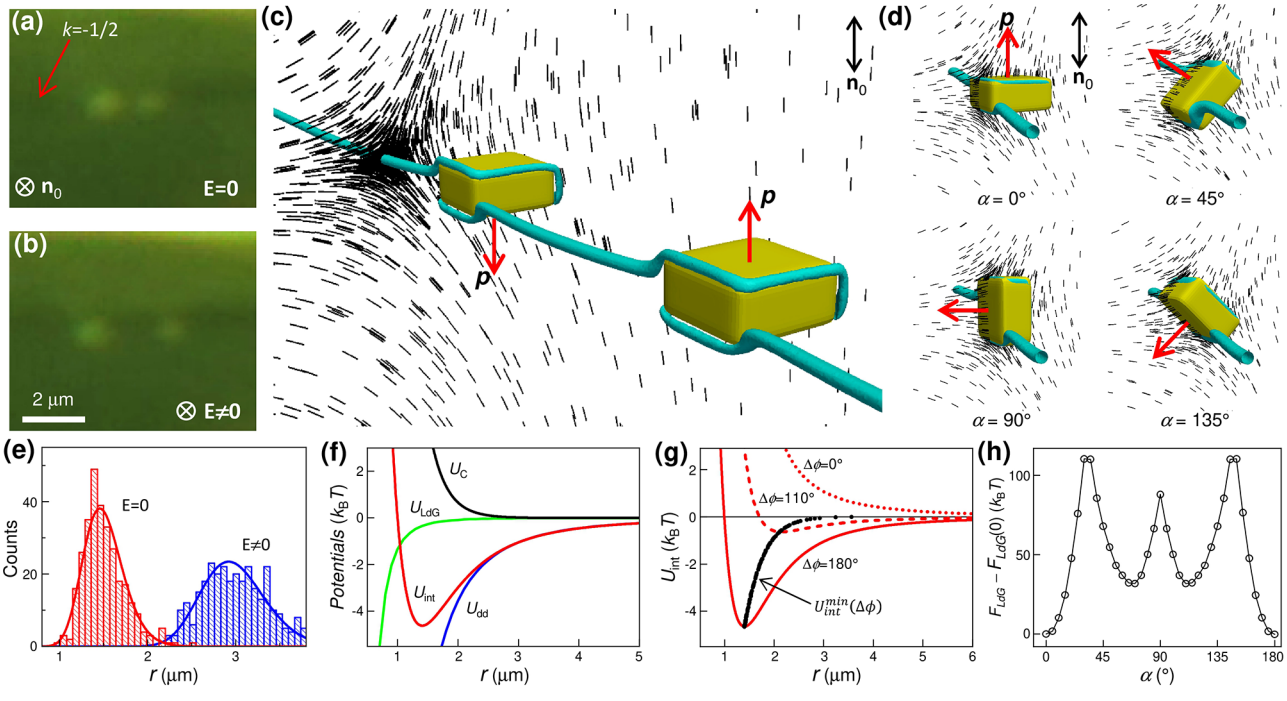

Figure 5. Electric control of interactions between ferroelectric nanoparticles with homeotropic anchoring in a defect line. (a,b) Dark-field microscopy images of two nanoparticles in a defect line without (a) and with (b) an applied field $E = 50$ mV/μm. (c) Numerical simulation of $\mathbf{n}(\mathbf{r})$ and a defect line around two nanoparticles with antiparallel dipoles at the shortest r. (d) Computer-simulated structures of $\mathbf{n}(\mathbf{r})$ around the nanoparticles at different orientations of $\mathbf{p}$ (red arrows) relative to the uniform background on the right side of the defect. (e) Histogram of separation between two nanoparticles depending on the orientation of dipoles without (red, anti-parallel dipoles) and with (blue) an applied field $E = 50$ mV/μm. (f) Interaction potentials calculated based on experimental separation histograms (e) for nanoparticles with antiparallel dipoles and computer-simulated U_{LdG}. (g) U_{int} for nanoparticles with dipoles $\mathbf{p}$ at $\Delta\phi = 180°$, 110°, and 0°. Black symbols show the shifting minimum of U_{int} versus $\Delta\phi$ changing within 180−90°. (h) Relative elastic free energy calculated for a nanoparticle trapped in the disclination at different orientation of $\mathbf{p}$ with respect to $\mathbf{n}_0$, with the energy of the equilibrium orientation subtracted.

https://dx.doi.org/10.1021/acs.nanolett.0c02087
Nano Lett. XXXX, XXX, XXX−XXX

the colloidal surface-induced defects (which can be controlled by surface functionalization) and director distortions in defining this behavior.

The electrostatic dipoles $\mathbf{p}\perp\mathbf{n}_0$ of nanoparticles with tangential boundary conditions can freely rotate around $\mathbf{n}_0$ (Figure 1h). Without applied field, the colloidal pair-interactions (Figure S5) are found to be typical for elastic quadrupoles because contributions of dipolar electrostatic interactions (Figure S6) average out and the monopole-type electrostatic interactions are only weakly anisotropic. Figure 3e shows a typical histogram of separations between pairs of nearest nanoparticles in a high concentration dispersion (Figure 1l) with two distinct peaks, which might correspond to different preferred orientations of electrostatic dipoles. Relatively large changes of separation between pairs of nanoparticles over time (Figure 3f) by 1−2 microns might be related to orientational thermal fluctuations of electrostatic dipoles and the ensuing changes of dipolar electrostatic interactions (Figure S6). Although these experiments reveal that "binding at a distance" between nanoparticles is weak and comparable in strength to thermal fluctuations, this binding arises from a highly complex interplay between elastic quadrupolar interactions with monopole- and dipole-type electrostatic interactions that depend on three-dimensional thermally driven motions, proximity of confining surfaces, relative orientations of electrostatic dipoles, and so on. Because this behavior of charged ferroelectric nanoparticles in the LC bulk is inherently complex even at the level of pair-interactions, we confine them into half-integer defect lines to unambiguously demonstrate that electrostatic interactions within LC are long-ranged and highly reconfigurable. One can measure the strength of colloidal pair-interactions between defect-entrapped nanoparticles by tracking their positions with the dark-field videomicroscopy. Because of the low Reynolds number (Re ≪ 1), inertia effects are negligible, and the interaction force is balanced by the viscous drag force F_S. Time-dependent center-to-center separation $r(t)$ between two nanoparticles moving within a defect line (Figure 4a,b) allows for determining the relative velocity $v(t) = dr/dt$ of nanoparticles and, consecutively, the separation-dependent interaction force and potential, as described in detail elsewhere.[19] Line defects were controllably created in homeotropic cells at ∼6 μm away from the surface of a round capillary used as a spacer (Figures 4 and 5). We numerically simulate $\mathbf{n}(\mathbf{r})$-configurations around nanoparticles in the proximity of such defects (Figures 4e and 5c,d) by numerical minimization of the Landau−de Gennes free energy. The Landau−de Gennes free energy functional[26] is expressed in terms of the traceless and symmetric order parameter tensor Q that acounts for nematic elasticity, variable nematic degree of order, and surface anchoring boundary conditions. Finite elements methods with adaptive meshing is used in order to acurately resolve the core regions of topological defects. Technical details on numerical implementation can be found in ref 27. Briefly, the phenomenological Landau−de Gennes free energy functional[26] F_{LdG} can be written in the following form

$$F_{LdG} = \int_V \left(aQ_{ij}^2 - bQ_{ij}Q_{jk}Q_{ki} + c(Q_{ij}^2)^2 + \frac{L_1}{2}\partial_k Q_{ij}\partial_k Q_{ij} + \frac{L_2}{2}\partial_j Q_{ij}\partial_k Q_{ik} \right) dV + W_p \int_{\partial V} f_s(Q_{ij}) dS \quad (1)$$

where $Q_{ij} = Q_{ji}$ $(i, j = 1, .., 3)$ is a traceless tensor order parameter and summation over repeated indices is assumed. In eq 1, the parameter a (unlike constants b and c) is assumed to depend linearly on temperature T as $a(T) = a_0(T - T^*)$, where a_0 is a material dependent constant, and T^* is the supercooling temperature of the isotropic phase. Phenomenological parameters L_1 and L_2 are related (via an uniaxial Ansatz for Q_{ij}) to the Frank−Oseen elastic constants. We describe planar degenerate anchoring, with the strength coefficient W_p of colloidal particles by using $f_s(Q_{ij}) = (\tilde{Q}_{ij} - \tilde{Q}_{ij}^{\perp})^2 + (\tilde{Q}_{ij}^2 - 3Q_b^2/2)^2$ with $\tilde{Q}_{ij} = Q_{ij} + Q_b\frac{\delta_{ij}}{2}$, $\tilde{Q}_{ij}^{\perp} = (\delta_{il} - \nu_i\nu_l)\tilde{Q}_{lk}(\delta_{kj} - \nu_k\nu_j)$ and with δ_{ij} being the Kronecker delta symbol, and $\mathbf{v}$ is the outward unit normal vector to the particle's surface;[28] $Q_b = b/8c(a + \sqrt{1 - {}^{64ac}/_{(3b^2)}})$ is the value of the scalar order parameter in the nematic phase, which is thermodynamically favored for $24ac/b_2 < 1$. Colloidal particle surfaces are defined to match the geometry of the corresponding experimental counterparts.[29,30]

Both experimental (Figures 4b and 5a,b) and modeling (Figures 4e and 5c,d) results agree that ferroelectric nanoparticles are trapped by the defect line to minimize the overall LC's free energy[31−34] and diffuse freely along its length. The $\mathbf{n}(\mathbf{r})$ around the defect defines the energy-minimizing preferred orientation of the colloidal inclusions (Figures 4e and 5c,d,h). The equilibrium internanoparticle distance r is determined by the overall interaction potential U_{tot}

$$U_{tot} = U_{int} + U_{ext} \quad (2)$$

where the pair-interactions between two colloidal nanoparticles are expressed by the first term $U_{int} = U_C + U_{Cd} + U_{dd} + U_{LdG}$, which is a sum of potentials for elastic pair-interactions U_{LdG}, screened dipole−dipole U_{dd}, and Coulomb U_C potentials with a cross term U_{Cd} of electrostatic monopole−dipole pair-interactions:[35,36]

$$U_C = \frac{(Ze)^2}{4\pi\varepsilon_0\bar{\varepsilon}}\frac{\exp(2\kappa R_{eq})}{(1 + \kappa R_{eq})^2}\frac{\exp(-\kappa r)}{r} \quad (3)$$

$$U_{Cd} = -C(r)A(r)Ze\frac{\mathbf{p}\cdot\mathbf{e}}{r^2} \quad (4)$$

$$U_{dd} = -C(r)\frac{A(r)(\mathbf{p}_1\cdot\mathbf{p}_2) - 3B(r)(\mathbf{p}_1\cdot\mathbf{e})(\mathbf{p}_2\cdot\mathbf{e})}{r^3} \quad (5)$$

with

$$A(r) = 1 + \kappa r \qquad B(r) = 1 + \kappa r + \frac{1}{3}(\kappa r)^2$$
$$C(r) = \frac{1}{4\pi\varepsilon_0\bar{\varepsilon}}\exp(-\kappa r) \quad (6)$$

where R_{eq} is a radius of equivalent sphere of a volume equal to a nanoparticle's volume w^2h, $\bar{\varepsilon}$ is an average dielectric constant of LC, $\mathbf{e} = \mathbf{r}/r$ is a unit vector pointing between the interacting nanoparticles. The second term in eq 2 $U_{ext} = -(\mathbf{p}_1\cdot\mathbf{E} + \mathbf{p}_2\cdot\mathbf{E}) = -E(p_1 + p_2\cos\Delta\phi)$ takes into account the coupling between electrostatic dipole orientations and external electric field $\mathbf{E}$ applied between electrodes, where $\Delta\phi$ is an angle between dipole moments of two nanoparticles.

While the defect line effectively terminates and re-emerges at diagonally opposite corners of colloidal nanoprisms with tangential boundary conditions (Figure 4e), such a defect

https://dx.doi.org/10.1021/acs.nanolett.0c02087
Nano Lett. XXXX, XXX, XXX−XXX

line continuously winds around nanoparticles with perpendicular boundary conditions (Figure 5c,d), somewhat resembling what was observed for larger colloidal particles within the LC bulk.[23−25] However, interactions due to minimizing the Landau−de Gennes free energy are short-ranged and weak compared to electrostatic interactions in both cases. Considering the particle shape with a mirror symmetry plane perpendicular to **p**, orientations of electrostatic dipoles can be parallel or antiparallel for the same elastic energy minimum (Figures 4e and 5c,d,h), though the electrostatic energy in this geometry is minimized for antiparallel **p**-orientations (Figure S6). Histograms in Figures 4f and 5e show that the center-to-center distance r can be tuned by electrically changing relative orientations of **p**-moments, with the shortest r corresponding to antiparallel **p**, when the dipole−dipole screened electrostatic potential U_{dd} (eq 5) is attractive at no external fields. Larger separations are obtained when these dipoles rotate away from antiparallel orientations (Figures 4f−i and 5e−g), though this field-induced nanoparticle rotation is resisted by elasticity-mediated alignment of the rectangular prisms within the defect line (shown in Figure 5h for perpendicular boundary conditions on the nanoparticle's surface), with U_{dd} remaining attractive within $\Delta\phi = 90-180°$ (Figures 4g−i and 5e−g). The energy-minimizing r is determined by minimization of the overall interaction potential U_{int} (Figures 4g−i and 5e−g). During field-induced nanoparticle rotation, U_{LdG} is further modified by additional perturbations of LC order caused by the rotation away from the initial U_{LdG}-minimizing orientations. However, the free energy associated with coupling of dipoles with external field $\sim 1200 k_B T$ is larger than the energetic barriers associated with rotating the nanoparticle around the defect line $\sim 120 k_B T$ (Figure 5h), consistent with our experiments that reveal such behavior. Since U_C is always repulsive and numerically calculated U_{LdG} is relatively short-range attractive, the separation between nanoparticles strongly depends on relative orientation of electrostatic dipoles. For dipoles rotating in a plane orthogonal to the disclination (Figure 4e), interaction potentials (Figures 4g−i and 5e−g) calculated based on experimental data (Figures 4f and 5e) show that the minimum of U_{int} shallows and shifts to larger separations as $\Delta\phi$ departs from antiparallel orientation at $\Delta\phi = 180°$. Calculated pair-interactions potential depends on relative orientations of the **p**-moments (Figures 4g,h and 5f,g), consistent with experiments.

While nematic colloids offer a means of controlling mesoscale nanoparticle self-assembly via changing particles' surface boundary conditions,[6,7] shape,[19] topology,[37] and chirality,[38] these interactions commonly result in assemblies with interparticle distances comparable to their size. The recent advent of charged nematic nanocolloids[15,16] offered the possibility of forming colloidal low-symmetry crystals and mesophases by balancing long-range electrostatic and elastic interactions, so that triclinic crystals with low nanoparticle packing fractions,[15] ferromagnetic fluids with various symmetries,[12,13] and even orthorhombic biaxial nematics[16] could be realized. However, these nanostructured soft materials still lack reliable means for reconfiguring their orientational and positional order of constituent nanoparticles, even though electric or magnetic fields could be applied to trigger facile realignment of the LC director of the nematic host medium.[39,40] Our findings above indicate that, under the right conditions, such long-range electrostatic interactions can lead to ferroelectric analogs of colloidal crystals[15] and polar uniaxial[12,14] and biaxial ferromagnetic LCs.[13] Furthermore, it may even be possible to dynamically reconfigure them by rotating ferroelectric dipolar nanoparticles and, through that, altering symmetries of crystals and mesophases. Changes of equilibrium interparticle distances by weak electric fields would lead to giant electrostriction[15] and could be a basis for new electrooptic applications. Furthermore, the electrostatic effects due to LC colloids can be further enriched by their interplay with gelation,[41] LC's flexoelectricity, electrostatics-controlled surface anchoring and separation of counterions by topological defect lines,[42−44] as well as by out-of-equilibrium elastic interactions.[8]

To conclude, electrostatically reconfigurable diffusion and pair-interactions between ferroelectric nanoparticles, in the bulk and when one-dimensionally confined by defect lines, indicate that electrostatic dipoles allow for a facile reconfiguration of LC colloidal behavior. The interparticle distances over an order of magnitude larger than the nanoparticle size can be controlled by vanishingly weak electric fields, potentially paving the road to electrically tunable self-assembly of colloidal crystals[15] and low-symmetry LC mesophases, as well as various technological applications.

■ ASSOCIATED CONTENT

Supporting Information

The Supporting Information is available free of charge at https://pubs.acs.org/doi/10.1021/acs.nanolett.0c02087.

SEM imaging; Ferroelectric nanoparticles and induced director structures versus their orientations; Ferroelectric microparticles and metastable colloidal structures; Interactions between nanoparticles; Multipolar electrostatic and elastic interactions (PDF)

■ AUTHOR INFORMATION

Corresponding Author

Ivan I. Smalyukh − *Department of Physics and Soft Materials Research Center and Department of Electrical, Computer, and Energy Engineering, Materials Science and Engineering Program, University of Colorado, Boulder, Colorado 80309, United States; Renewable and Sustainable Energy Institute, National Renewable Energy Laboratory and University of Colorado, Boulder, Colorado 80309, United States;* orcid.org/0000-0003-3444-1966; Email: ivan.smalyukh@colorado.edu

Authors

Blaise Fleury − *Department of Physics and Soft Materials Research Center, University of Colorado, Boulder, Colorado 80309, United States;* orcid.org/0000-0002-5408-5789

Bohdan Senyuk − *Department of Physics and Soft Materials Research Center, University of Colorado, Boulder, Colorado 80309, United States*

Mykola Tasinkevych − *Departamento de Física, Faculdade de Ciências and Centro de Física Teórica e Computacional, Universidade de Lisboa, 1649-004 Lisboa, Portugal*

Complete contact information is available at: https://pubs.acs.org/10.1021/acs.nanolett.0c02087

Notes

The authors declare no competing financial interest.

https://dx.doi.org/10.1021/acs.nanolett.0c02087
Nano Lett. XXXX, XXX, XXX−XXX

■ ACKNOWLEDGMENTS

We acknowledge discussions with Q. Liu and H. Mundoor and funding from the US Department of Energy, Office of Basic Energy Sciences, Division of Materials Sciences and Engineering, contract DE-SC0019293 with the University of Colorado Boulder. M.T. acknowledges financial support from the Portuguese Foundation for Science and Technology under Contracts No. IF/00322/2015, UID/FIS/00618/2019 and PTDC/FIS-MAC/28146/2017 (LISBOA-01-0145-FEDER028146). I. I. S. also acknowledges the hospitality of the Kavli Institute for Theoretical Physics at the University of California, Santa Barbara, where he was working on this publication during his extended stay and where his research was supported in part by the U.S. National Science Foundation under Grant No. NSF PHY-1748958.

■ REFERENCES

(1) Chaikin, P. M.; Lubensky, T. C. *Principles of Condensed Matter Physics*; Cambridge University Press: Cambridge, 2000.
(2) Israelachvili, J. *Intermolecular and Surface Forces*; Academic Press: London, 1991.
(3) Verwey, E. J. W.; Overbeek, J. Th. G. *Theory of Stability of Lyophobic Colloid*; Elsevier: Amsterdam, 1948.
(4) Chen, S. H. Small angle neutron scattering studies of the structure and interaction in micellar and microemulsion systems. *Annu. Rev. Phys. Chem.* **1986**, *37*, 351−399.
(5) Bonnet-Gonnet, C.; Belloni, L.; Cabane, B. Osmotic pressure of latex dispersions. *Langmuir* **1994**, *10*, 4012−4021.
(6) Poulin, P.; Stark, H.; Lubensky, T. C.; Weitz, D. A. Novel colloidal interactions in anisotropic fluids. *Science* **1997**, *275*, 1770−1773.
(7) Smalyukh, I. I. Liquid crystal colloids. *Annu. Rev. Condens. Matter Phys.* **2018**, *9*, 207−226.
(8) Yuan, Y.; Liu, Q.; Senyuk, B.; Smalyukh, I. I. Elastic colloidal monopoles and reconfigurable self-assembly in liquid crystals. *Nature* **2019**, *570*, 214−218.
(9) Lubensky, T. C.; Pettey, D.; Currier, N.; Stark, H. Topological defects and interactions in nematic emulsions. *Phys. Rev. E: Stat. Phys., Plasmas, Fluids, Relat. Interdiscip. Top.* **1998**, *57*, 610−625.
(10) Senyuk, B.; Puls, O.; Tovkach, O. M.; Chernyshuk, S. B.; Smalyukh, I. I. Hexadecapolar colloids. *Nat. Commun.* **2016**, *7*, 10659.
(11) Senyuk, B.; Aplinc, J.; Ravnik, M.; Smalyukh, I. I. High-order elastic multipoles as colloidal atoms. *Nat. Commun.* **2019**, *10*, 1825.
(12) Mertelj, A.; Lisjak, D.; Drofenik, M.; Čopič, M. Ferromagnetism in suspensions of magnetic platelets in liquid crystal. *Nature* **2013**, *504*, 237−241.
(13) Liu, Q.; Ackerman, P. J.; Lubensky, T. C.; Smalyukh, I. I. Biaxial ferromagnetic liquid crystal colloids. *Proc. Natl. Acad. Sci. U. S. A.* **2016**, *113*, 10479−10484.
(14) Brochard, F.; de Gennes, P. G. Theory of magnetic suspensions in liquid crystals. *J. Phys. (Paris)* **1970**, *31*, 691−708.
(15) Mundoor, H.; Senyuk, B.; Smalyukh, I. I. Triclinic nematic colloidal crystals from competing elastic and electrostatic interactions. *Science* **2016**, *352*, 69−73.
(16) Mundoor, H.; Park, S.; Senyuk, B.; Wensink, H. H.; Smalyukh, I. I. Hybrid molecular-colloidal liquid crystals. *Science* **2018**, *360*, 768−771.
(17) Reznikov, Y.; Buchnev, O.; Tereshchenko, O.; Reshetnyak, V.; Glushchenko, A.; West, J. Ferroelectric nematic suspension. *Appl. Phys. Lett.* **2003**, *82*, 1917−1919.
(18) Li, F.; Buchnev, O.; Cheon, C.; Glushchenko, A.; Reshetnyak, V.; Reznikov, Y.; Sluckin, T. J.; West, J. Orientational coupling amplification in ferroelectric nematic colloids. *Phys. Rev. Lett.* **2006**, *97*, 147801.
(19) Lapointe, C. P.; Mason, T. G.; Smalyukh, I. I. Shape-controlled colloidal interactions in nematic liquid crystals. *Science* **2009**, *326*, 1083−1086.
(20) Chao, C.; Ren, Z.; Zhu, Y.; Xiao, Z.; Liu, Z.; Xu, G.; Mai, J.; Li, X.; Shen, G.; Han, G. Self-templated synthesis of single-crystal and single-domain ferroelectric nanoplates. *Angew. Chem., Int. Ed.* **2012**, *51*, 9283−9287.
(21) *Principles and Applications of Ferroelectrics and Related Materials*; Lines, M. E.; Glass, A. M., Eds.; Clarendon Press: Oxford, 1977.
(22) Loudet, J. C.; Hanusse, P.; Poulin, P. Stokes drag on a sphere in a nematic liquid crystal. *Science* **2004**, *306*, 1525−1525.
(23) Phillips, P. M.; Rey, A. D. Texture formation mechanisms in faceted particles embedded in a nematic liquid crystal matrix. *Soft Matter* **2011**, *7*, 2052−2063.
(24) Beller, D. A.; Gharbi, M. A.; Liu, I. B. Shape-controlled orientation and assembly of colloids with sharp edges in nematic liquid crystals. *Soft Matter* **2015**, *11*, 1078−1086.
(25) Senyuk, B.; Liu, Q.; Yuan, Y.; Smalyukh, I. I. Edge pinning and transformation of defect lines induced by faceted colloidal rings in nematic liquid crystals. *Phys. Rev. E: Stat. Phys., Plasmas, Fluids, Relat. Interdiscip. Top.* **2016**, *93*, No. 062704.
(26) de Gennes, P. G.; Prost, J. *The Physics of Liquid Crystals*, 2nd ed.; Oxford University Press, Inc.: New York, 1993.
(27) Tasinkevych, M.; Silvestre, N. M.; Telo da Gama, M. M. Liquid crystal boojum-colloids. *New J. Phys.* **2012**, *14*, No. 073030.
(28) Fournier, J. B.; Galatola, P. Modeling planar degenerate wetting and anchoring in nematic liquid crystals. *Europhys. Lett.* **2005**, *72*, 403−409.
(29) In our calculations, we use $a_0 = 0.044 \times 10^6$ J m^{-3}, $b = 0.816 \times 10^6$ J m^{-3}, $c = 0.45 \times 10^6$ J m^{-3}, $L_1 = 6 \times 10^{12}$ J m^{-1}, and $L_2 = 12 \times 10^{12}$ J m^{-1}, which are typical values for 5CB at $T^* = 307$ K. For these values of the model parameters, the bulk correlation length $\zeta = 2[2c(3L_1 + 2L_2)]^{1/2}/b \approx 15$ nm at the isotropic−nematic coexistence, $24ac/b^2 = 1$.
(30) Chandrasekhar, S. *Liquid Crystals*, 2nd ed.; Cambridge University Press: Cambridge, 1992.
(31) Martinez, A.; Hermosillo, L.; Tasinkevych, M.; Smalyukh, I. I. Linked topological colloids in a nematic host. *Proc. Natl. Acad. Sci. U. S. A.* **2015**, *112*, 4546−4551.
(32) Wang, X.; Miller, D. S.; Bukusoglu, E.; de Pablo, J. J.; Abbott, N. L. Topological defects in liquid crystals as templates for molecular self-assembly. *Nat. Mater.* **2016**, *15*, 106−112.
(33) Pires, D.; Fleury, J.-B.; Galerne, Y. Colloid particles in the interaction field of a disclination line in a nematic phase. *Phys. Rev. Lett.* **2007**, *98*, 247801.
(34) Senyuk, B.; Evans, J. S.; Ackerman, P.; Lee, T.; Manna, P.; Vigderman, L.; Zubarev, E. R.; van de Lagemaat, J.; Smalyukh, I. I. Shape-dependent oriented trapping and scaffolding of plasmonic nanoparticles by topological defects for self-assembly of colloidal dimers in liquid crystals. *Nano Lett.* **2012**, *12*, 955.
(35) Tsonchev, S.; Schatz, G.; Ratner, M. A. Screened multipole electrostatic interactions at the Debye−Hückel level. *Chem. Phys. Lett.* **2004**, *400*, 221−225.
(36) Maciejczyk, M.; Spasic, A.; Liwo, A.; Scheraga, H. A. DNA duplex formation with a coarse-grained model. *J. Chem. Theory Comput.* **2014**, *10*, 5020−5035.
(37) Senyuk, B.; Liu, Q.; He, S.; Kamien, R. D.; Kusner, R. B.; Lubensky, T. C.; Smalyukh, I. I. Topological colloids. *Nature* **2013**, *493*, 200−205.
(38) Yuan, Y.; Martinez, A.; Senyuk, B.; Tasinkevych, M.; Smalyukh, I. I. Chiral liquid crystal colloids. *Nat. Mater.* **2018**, *17* (17), 71−79.
(39) Liu, Q.; Yuan, Y.; Smalyukh, I. I. Electrically and optically tunable plasmonic guest−host liquid crystals with long-range ordered nanoparticles. *Nano Lett.* **2014**, *14*, 4071−4077.
(40) Zhang, Y.; Liu, Q.; Mundoor, H.; Yuan, Y.; Smalyukh, I. I. Metal nanoparticle dispersion, alignment, and assembly in nematic liquid crystals for applications in switchable plasmonic color filters and E-polarizers. *ACS Nano* **2015**, *9*, 3097−3108.
(41) Wood, T. A.; Lintuvuori, J. S.; Schofield, A. B.; Marenduzzo, D.; Poon, W. C. A self-quenched defect glass in a colloid-nematic liquid crystal composite. *Science* **2011**, *334*, 79−83.

https://dx.doi.org/10.1021/acs.nanolett.0c02087
Nano Lett. XXXX, XXX, XXX−XXX

(42) Meyer, R. B. Piezoelectric effects in liquid crystals. *Phys. Rev. Lett.* **1969**, *22*, 918−921.
(43) Mundoor, H.; Senyuk, B.; Almansouri, M.; Park, S.; Fleury, B.; Smalyukh, I. I. Electrostatically controlled surface boundary conditions in nematic liquid crystals and colloids. *Sci. Advances* **2019**, *5*, eaax4257.
(44) Tatarkova, S. A.; Burnham, D. R.; Kirby, A. K.; Love, G. D.; Terentjev, E. M. Colloidal interactions and transport in nematic liquid crystals. *Phys. Rev. Lett.* **2007**, *98*, 157801.

https://dx.doi.org/10.1021/acs.nanolett.0c02087
Nano Lett. XXXX, XXX, XXX−XXX